The Astrophysical Journal, 931:133 (13pp), 2022 June 1 https://doi.org/10.3847/1538-4357/ac66de

S-type Stars Discovered in Medium-resolution Spectra of LAMOST DR9

Jing Chen[1,2], A-Li Luo[1,2,3], Yin-Bi Li[1,2], Xiang-Lei Chen[1,2], Rui Wang[1], Shuo Li[1,2], Bing Du[1], and Xiao-Xiao Ma[1,2]
[1] CAS Key Laboratory of Optical Astronomy, National Astronomical Observatories, Beijing 100101, People's Republic of China; lal@nao.cas.cn, ybli@bao.ac.cn
[2] University of Chinese Academy of Sciences, Beijing 100049, People's Republic of China
[3] School of Information Management & Institute for Astronomical Science, Dezhou University, Dezhou 253023, People's Republic of China
Received 2022 February 15; revised 2022 April 10; accepted 2022 April 11; published 2022 June 2

Abstract

In this paper, we report on 606 S-type stars identified from Data Release 9 of the LAMOST medium-resolution spectroscopic (MRS) survey; 539 of them are reported for the first time. The discovery of these stars is a three-step process, i.e., selecting with ZrO-band indices greater than 0.25, excluding non-S-type stars with the iterative Support Vector Machine method, and finally retaining stars with absolute bolometric magnitude larger than −7.1. The 606 stars are consistent with the distribution of known S-type stars in the color–magnitude diagram. We estimated the C/Os using the [C/Fe] and [O/Fe] provided by APOGEE and the MARCS model for S-type stars, respectively, and the results of the two methods show that the C/Os of all stars are larger than 0.5. Both the locations on the color–magnitude diagram and C/Os further verify the nature of our S-type sample. Investigating the effect of TiO and atmospheric parameters on ZrO with the sample, we found that log g has a more significant impact on ZrO than $T_{\rm eff}$ and [Fe/H], and both TiO and log g may negatively correlate with ZrO. According to the criterion of Tian et al., a total of 238 binary candidates were found by the zero-point-calibrated radial velocities from the officially released catalog of LAMOST MRS and the catalog of Zhang et al. A catalog of these 606 S-type stars is available from the following link: doi.org/10.12149/101097.

Unified Astronomy Thesaurus concepts: S stars (1421)

Supporting material: machine-readable table

1. Introduction

S-type stars were originally defined by Merrill (1922), and their spectra show characteristics of s-process element enrichments (especially strong ZrO bands; Keenan 1954; Smith & Lambert 1990), which are produced through the third dredge-up process in the thermally pulsing asymptotic giant branch (TP-AGB) stage. S-type stars can be classified into two categories, i.e., intrinsic and extrinsic S-type stars. Intrinsic S-type stars are most likely to be members of TP-AGB stars and have technetium lines in their spectra (Tc-rich S-type stars). Extrinsic S-type stars, without Tc lines in their optical spectra (Tc-poor S-type stars), are in a binary system, and their s-process overabundances were caused by the mass transfer of a former AGB companion, which is a white dwarf now (Jorissen & Mayor 1988).

As a type of AGB star, S-type stars are at the intermediate evolutionary stage between M-type giants (C/O < 0.5) and carbon stars (C/O > 1.0) (Iben & Renzini 1983), and the atmospheres of AGB stars are characterized by an increasing enrichment of ^{12}C and s-process elements, which increase along the spectral sequence M-MS-S-SC-C. MS stars are typically at C/O = 0.5 to 0.7, S stars are above this range and up to more than 0.95, and SC stars represent a rare but important transition group between S stars and carbon stars. Different from M giants and carbon stars, S-type stars (MS, S, and SC) have not been well studied, and it is undoubtedly important for understanding the evolutionary stage from M giants to carbon stars and helping to clarify the s-processes taking place inside stars.

Searches in survey observations have yielded catalogs of S-type stars, such as the Henize sample (Henize 1960) and the three versions of the General Catalogue of S stars (hereafter GCSS; Stephenson 1976, 1984, 1990). Henize (1960) provided a sample of 205 S stars located south of $\delta = -25°$ and brighter than $R = 10.5$, which were inherited by Van Eck et al. (2000). Stephenson (1976) constructed the first version of GCSS including 741 S-type stars, and Stephenson (1984) listed all the 1347 S-type stars whose positions were known at that time, which is nearly twice as large as the first version in Stephenson (1976). Furthermore, Stephenson (1990) published the latest version of GCSS including 75 new and fainter S stars located in the northern Milky Way. The Henize sample was used to investigate the properties of the S stars, such as technetium dichotomy, the proportion of extrinsic and intrinsic S stars, and new symbiotic stars (Van Eck & Jorissen 1999, 2000; Van Eck et al. 2000). Shetye et al. (2018, 2019, 2020) used the GCSS to study the stellar parameters and chemical abundances of S-type stars and found evidence for the third dredge-up occurrence in S-type stars and the case of bitrinsic S-type stars. Chen et al. (2019) used GCSS to investigate their infrared properties and found 172 new intrinsic S-type stars.

The atmospheric parameters of S-type stars are difficult to determine because their atmospheric structure is not only related to the effective temperature, surface gravity, and metallicity but is also sometimes severely impacted by the C/O and even more by the elements of the s-process abundance. However, some previous works still tried to estimate the atmospheric parameter for S-type stars. The ($V - K$, $J - K$) and (TiO, ZrO) diagnostics can be used to estimate the atmospheric parameters of S-type stars in Plez

et al. (2003), such as $T_{\rm eff}$, C/O, [Fe/H], and [s/Fe]. MARCS models were published covering the entire parameter space of S-type stars (Plez et al. 2003; Gustafsson et al. 2008; Van Eck et al. 2017), and Shetye et al. (2018, 2019, 2020) used these models and HERMES spectra (Raskin et al. 2011) to calculate the element abundances of some S-type stars.

Most S-type stars in the above catalogs are mainly from the southern sky and outside of galactic latitude region $\pm 10°$. As a survey of the northern sky, the Large Sky Area Multi-object Fiber Spectroscopic Telescope (LAMOST) can undoubtedly increase the samples of S-type stars, which will provide more information for further studies. In this work, we searched, identified, and analyzed S-type stars using the Ninth Data Release (DR9) medium-resolution spectra (MRS) from LAMOST. This paper is organized as follows. The methods for searching S-type stars are presented in Section 2, and further identification is introduced in Section 3. In Section 4, we discussed the relationship of ZrO versus TiO and ZrO versus atmospheric parameters, and selected binary candidates with radial velocities. Finally, the summary is presented in Section 5.

2. Data

2.1. LAMOST and Gaia

LAMOST is a 4 m Schmidt telescope, which is equipped with 4000 fibers in a field of view of 20 deg^2 in the sky (Wang et al. 1996; Su & Cui 2004; Zhao et al. 2006; Cui et al. 2012; Luo et al. 2012; Zhao et al. 2012). In 2018 October, LAMOST started the phase II survey, which contains both low- and medium-resolution spectroscopic surveys. In 2020 June, LAMOST delivered its eighth data release (DR8), which provides 17,628,024 single exposure and 4,728,861 coadded MRS. From September 2020 to June 2021, LAMOST collected an additional 6,054,085 single-exposure spectra and 1,724,868 combined spectra, which will be officially released in March of this year as part of DR9.[4] For an MRS target, there are two spectra within one exposure, i.e., a blue- and red-band spectra, their wavelength ranges are 4950–5350 Å and 6300–6800 Å, and they both have a resolution of 7500 respectively at 5163 Å (blue) and 6593 Å (red). In this data release, five spectroscopic parameter catalogs are published; the LAMOST MRS General Catalog was used in this work.

Gaia is the space-astrometry mission of the European Space Agency, and the primary science goal of Gaia is to examine the kinematical, dynamical, and chemical structure and evolution of our Milky Way (Gaia Collaboration et al. 2016). The science data of Gaia comprise absolute astrometry (positions, proper motions, and parallaxes), as well as three broadband photometries (G band, $G_{\rm BP}$, and $G_{\rm RP}$) for all objects. Gaia data release 2 (DR2) provides precise positions, proper motions, parallaxes, and photometries for over 1.3 billion stars brighter than magnitude 21 (Gaia Collaboration et al. 2018).

2.2. Sample Selection of Low-temperature Giants

S-type stars are low-temperature giants, and we first selected such a sample of giants from LAMOST DR9. However, as there were neither stellar parameters nor stellar types in the LAMOST MRS General Catalog, the low-temperature giants were selected from the color–magnitude diagram. As listed in Table 1, we collected 2755 S-type stars from eight catalogs in the literature, which include the four catalogs mentioned in Section 1. They were then cross-matched with Gaia DR2, and only 1076 stars with $\sigma_\varpi/\varpi \leqslant 0.3$ were retained.

The distribution of the 1076 stars on the color–magnitude diagram of Gaia is shown in Figure 1, and the absolute magnitude M_G was calculated by

$$M_G = G + 5 - 5\log_{10} r - A_G, \tag{1}$$

where G is the Gaia G magnitude, r is heliocentric distance, and A_G is extinction. r was simply estimated by inverting the parallax, and the parallax zero-point, which may range from -29 μas to -80 μas as mentioned in Zinn et al. (2019), was not considered. In addition, A_G was also not considered because the individual Gaia extinction estimates are rather poor for most stars.

From Figure 1, we can see that most S-type stars are distributed on the upper right of the red dashed line although a small number of them fall on the main sequence, thus we select the low-temperature giants with the color and magnitude criteria shown by the red dashed lines as follows:

$$M_G > 5 \cdot (G_{\rm BP} - G_{\rm RP})/9 - 1, \tag{2}$$

$$G_{\rm BP} - G_{\rm RP} \geqslant 1.6, \tag{3}$$

where $G_{\rm BP}$ and $G_{\rm RP}$ are the blue- and red-band magnitudes of Gaia, respectively.

The LAMOST MRS General Catalog was cross-matched with Gaia DR2 using a radius of 3″, and 29,040,187 spectra have Gaia data. Using the above criteria in Equations (2) and (3), a sample of 1,099,403 spectra of low-temperature giants were selected.

2.3. Band-strength Indices

As in Keenan (1954), the absorption from the ground state of the ZrO molecule gives rise to three band systems, the α-system in blue, β-system in yellow, and γ-system in red. According to the LAMOST MRS wavelength range introduced in Section 2.1, the γ-system in the red-band spectra was used, we selected the four most intense ZrO molecular bands of the γ-system according to Ake (1979), and their wavelength ranges in Gałan et al. (2019) are slightly changed after considering the much higher spectral resolution of LAMOST MRS.

We calculated the ZrO-band strengths of S-type stars and M giants to verify whether there is a difference between the two types of stars. The band-strength indices were computed as follows:

$$B = 1 - \frac{\lambda_{C,f} - \lambda_{C,i}}{\lambda_{B,f} - \lambda_{B,i}} \frac{\int_{\lambda_{B,i}}^{\lambda_{B,f}} F_\lambda d\lambda}{\int_{\lambda_{C,i}}^{\lambda_{C,f}} F_\lambda d\lambda}, \tag{4}$$

where F_λ is the observed flux in the wavelength range (λ, $\lambda + d\lambda$), and the continuum window $\lambda_{C,f} - \lambda_{C,i}$ and the band window $\lambda_{B,f} - \lambda_{B,i}$, which were introduced in Gałan et al. (2019), are listed in Table 2.

The spectra of S-type stars were obtained by cross-matching all catalogs in Table 1 with the LAMOST DR9 MRS, and the common source numbers are listed in the fifth column of Table 1. In addition, only the S-type stars with relatively good quality and obvious ZrO were retained, which are listed in the last column of Table 1. Because there are common sources

[4] http://www.lamost.org/dr9/

Table 1
The Number of S-type Stars in the Literature

Reference	Number[a]	$\text{Xmatch}_{\text{Gaia}}$ [b]	Gaia Selected[c]	$\text{Xmatch}_{\text{LAMOST}}$ [d]	LAMOST Selected[e]
Keenan (1954)	87	87	75	10	2
Blanco & Nassau (1957)	29	29	19	3	2
Henize (1960)	199	199	184	0	0
Dolidze (1975)	73	73	54	29	18
Stephenson (1976)	741	263	178	37	0
MacConnell (1979)	204	204	189	1	1
Stephenson (1984)	1347	487	348	31	27
Stephenson (1990)	75	75	29	2	1

Notes.
[a] The number of S-type stars in each reference.
[b] The number of S-type stars after matching with Gaia DR2 with 3″.
[c] The number of S-type stars with high qualities of Gaia parallax.
[d] The number of S-type stars after matching with LAMOST DR9 with 3″.
[e] The number of S-type stars with high spectral qualities of LAMOST DR9.

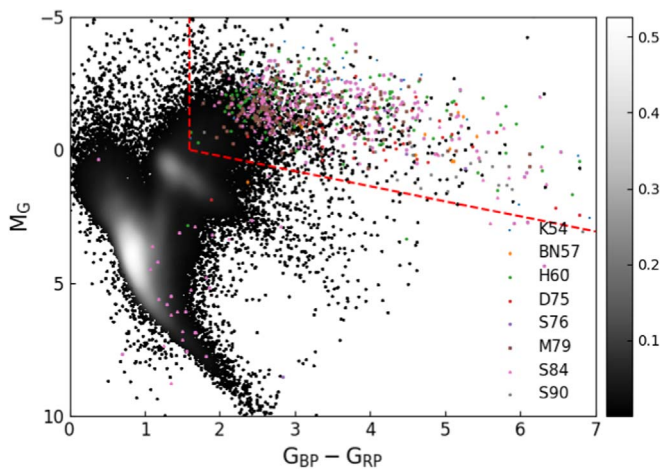

Figure 1. The location of the sample of low-temperature giants in the Hertzsprung–Russell diagram. The dots with different colors denote the known S-type stars in eight catalogs listed in Table 1, and the red dashed lines indicate the criterion for selecting the low-temperature-giant sample. The color-coded density distribution represents the background stars in common between LAMOST and Gaia.

between different S-type catalogs, we only kept the information from the latest catalog, and the final 460 spectra of 51 stars selected are listed in Table 3. The 200 spectra of M giants are from S. Li (2022, in preparation); we excluded the spectra with low signal-to-noise ratio (S/N) and incorrect radial velocity measurements. Using Equation (4), we calculated the ZrO-band indices for these S-type stars and M giants, and the distribution is shown in Figure 2.

As shown in Figure 2, the ZrO indices of a small fraction of M giants are in the region of S-type stars, we manually checked these spectra and found that they are M-giant spectra with low S/Ns or weak ZrO (but the calculated line index does indeed fall in this region) or S-type star spectra. Anyway, S-type stars and M-giant stars can be clearly distinguished with the ZrO-band indices, and we used the criterion of $B_{\text{ZrO}} > 0.25$ to distinguish S-type stars from M giants preliminarily. This criterion was applied to the 1,099,403 low-temperature giant spectra, and 21,121 red-band spectra of S-type candidates were obtained after removing the blue-band spectra.

Table 2
Boundaries of the Continuum and Band Windows of ZrO Used in the Computation of the Band Indices

Band	$\lambda_{B,i}$	$\lambda_{B,f}$	$\lambda_{C,i}$	$\lambda_{C,f}$
ZrO_1	6345.0	6352.0	6464.0	6472.0
ZrO_2	6378.0	6382.0	6464.0	6472.0
ZrO_3	6474.0	6479.0	6464.0	6472.0
ZrO_4	6508.0	6512.0	6464.0	6472.0

2.4. Selecting S-type Stars with the Iterative SVM Method

Because the number of selected known S-type stars in Table 3 is not large, we used the Support Vector Machine (SVM) algorithm, a supervised machine-learning algorithm for classification and regression (Cortes & Vapnik 1995), to classify S stars from LAMOST DR9 MRS. The advantage of SVM is that it is suitable for small samples, and the complexity of the calculation depends on the number of support vectors rather than on the dimensionality of the sample space.

Before training the SVM classifier, we preprocessed the MRS spectra using the following four steps. (1) In the LAMOST FITS file, the "ormask" flag was set for each wavelength to give six kinds of spectrum problems, and the wavelengths with "ormask" larger than 0 were removed. (2) Due to the limitation of the wavelength range of the MRS spectra, the ZrO bands are only present in the red-band spectra, so the red-band spectra were shifted to the vacuum wavelength using the radial velocity (RV) released by LAMOST. (3) The spectra were resampled in steps of 0.1 Å to facilitate the subsequent training of the model. (4) S-type stars are low-temperature giant stars with obvious molecular bands in their spectra, and removing the pseudo-continuum during normalization may obscure some features; thus, we used the maximum flux to normalize them. Figure 3 shows an example after spectral preprocessing for a red-band MRS spectrum.

In order to train and test the classifier, we need to decide the input features and training and test data sets. The S-type stars are defined by the existence of clearly detectable ZrO bands in visual spectra, and thus the previously defined four ZrO bands were adopted as the input features, which are shown in Table 2.

There are 51 S-type stars in Table 3 with LAMOST spectra, which have been observed many times, and their 460

Table 3
Basic Information of the 51 S-type Stars

Reference	Identifier[a]	Sptype[b]	LAMOST Designation	R.A.	Decl.
Keenan (1954)	HD 286892	S5.5/1	J043537.19+124145.6	68.904993	12.696
	V* V812 Oph	S5+/2.5	J174131.93+064341.3	265.38307	6.7281448
Blanco & Nassau (1957)	V* LZ Per	S	J033341.59+485941.5	53.423305	48.994888
	S1* 141	S	J061549.23+250040.5	93.955129	25.011262
Dolidze (1975)	[D75b] Star 9	S	J021852.44+624813.6	34.718531	62.803778
	[D75b] Star 10	MS	J021916.76+594221.6	34.819836	59.706
	[D75b] Star 13	MS	J022444.76+553545.5	36.186504	55.595997
	[D75b] Star 14	MS	J022519.33+581610.6	36.33057	58.26962
	[D75b] Star 28	MS	J045915.25+473601.1	74.813546	47.600324
	[D75b] Star 31	S	J051139.28+290621.3	77.913696	29.105927
	[D75b] Star 33	MS	J052837.34+340228.0	82.155593	34.041116
	[D75b] Star 36	MS	J053511.19+374546.0	83.796637	37.762804
	[D75b] Star 37	S	J053652.05+290215.5	84.216913	29.037664
	[D75b] Star 42	MS	J060237.80+290705.8	90.657512	29.118293
	[D75b] Star 43	MS	J060527.88+222042.3	91.366174	22.345094
	[D75b] Star 47	M2-MS	J061009.58+233301.0	92.539955	23.550281
	[D75b] Star 48	M3III-MS	J061034.57+233854.8	92.644077	23.648562
	[D75b] Star 49	MS	J061852.52+211216.0	94.718843	21.204468
	[D75b] Star 51	S	J063627.02+070033.1	99.112595	7.009203
	[D75b] Star 52	MS	J063903.22+023400.1	99.763447	2.566697
	[D75b] Star 53	S	J064356.36+014459.6	100.98486	1.7498975
	[D75b] Star 75	S	J204555.27+363218.6	311.48032	36.538501
MacConnell (1979)	MC79 1-19	S3:*4	J071737.44+002047.2	109.40603	0.3464478
Stephenson (1984)	CSS 28	S4,6e	J011941.97+723640.8	19.9249	72.61135
	CSS 63		J024440.21+530546.2	41.16757	53.09619
	CSS 73		J032809.69+174046.7	52.040411	17.679651
	CSS 96	S6,1	J042747.65+222120.0	66.94858	22.35556
	CSS 97	Swk	J042841.35+215035.1	67.172307	21.843089
	CSS 98	Swk	J042901.55+234648.6	67.256488	23.780182
	CSS 115		J045351.76+320435.7	73.46568	32.0766
	CSS 138	Swk	J052545.59+322401.4	81.439975	32.400405
	CSS 142		J053227.32+405843.8	83.11387	40.978855
	CSS 148		J053817.61+281144.2	84.573412	28.195633
	CSS 214		J062352.89+211830.1	95.9704	21.308366
	CSS 220		J062715.33+180423.6	96.813916	18.073228
	CSS 216		J062742.91+521547.1	96.928826	52.263103
	CSS 225		J063355.57+213204.2	98.481546	21.534523
	CSS 241		J064024.65+234358.4	100.10274	23.732894
	CSS 255		J064532.37+064706.2	101.38488	6.7850816
	CSS 257	M7wkS	J064646.93+264114.8	101.69558	26.687463
	CSS 273		J065425.98+054703.2	103.60827	5.7842395
	CSS 305	M3S	J070606.48-005239.5	106.52704	−0.8776633
	CSS 331		J072029.17+322317.6	110.12156	32.388246
	CSS 403	S4/4e	J074918.17+234404.0	117.32572	23.734467
	CSS 413	M4S	J075253.23+343650.8	118.2218	34.614128
	CSS 494	S3/6e	J082142.85+171705.3	125.42858	17.28483
	CSS 986		J172448.18+335508.4	261.20075	33.919
	CSS 1249		J205232.65+562440.6	313.13607	56.4113
	CSS 1310	S6/2	J224954.43+593935.2	342.47683	59.659802
	CSS 1328	SwK	J231608.42+285149.2	349.03511	28.863688
Stephenson (1990)	CSS2 75	S	J234430.41+560658.7	356.12675	56.11632

Notes.
[a] The identifier from SIMBAD.
[b] The spectral type from SIMBAD.

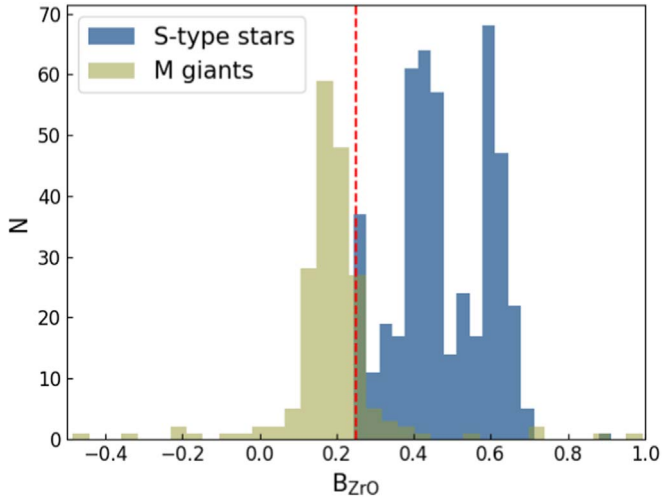

Figure 2. The histogram of the ZrO-band indices (B_{ZrO}). The blue and brown histograms represent the B_{ZrO} distributions for S-type stars and M giants, respectively, and the red dashed line denotes the location of $B_{ZrO} = 0.25$.

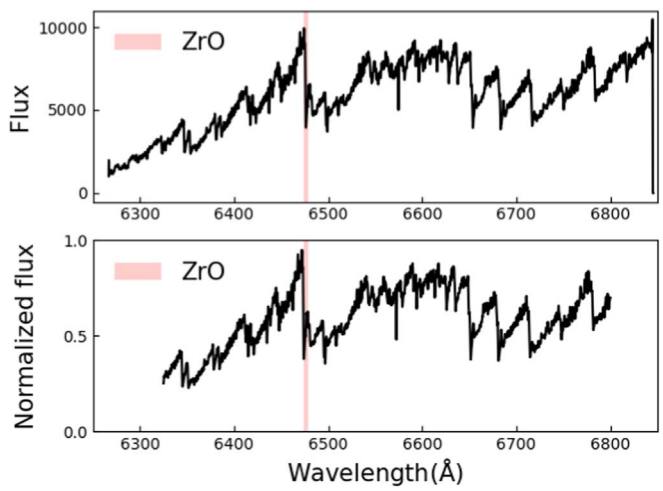

Figure 3. An example before (top) and after (bottom) spectral preprocessing for a red-band MRS spectrum.

single-exposure and coadded red-band spectra were treated as the positive samples. We randomly selected the same number of spectra from the low-temperature-giant sample as the negative sample and manually checked the their spectra to avoid the contaminations of S-type stars. The positive and negative samples were randomly divided into the training data set and test data set according to the ratio of 8:2 to train the SVM classifier and evaluate the performance of the model, respectively.

After training and testing, the SVM model was applied to select S-type star spectra from the 21,121 spectra of S-type candidates. The selection process of S-type stars was a gradual iterative process, in which the S-type stars selected in the previous round were used as the positive samples in the next round, the negative samples of the same size in each round were reselected, and the model was retrained until a few new S-type stars can be found.

In the first round, 2060 spectra were predicted as S-type stars; we manually checked these spectra, and 2039 spectra (339 stars) with high spectral quality were left as the positive

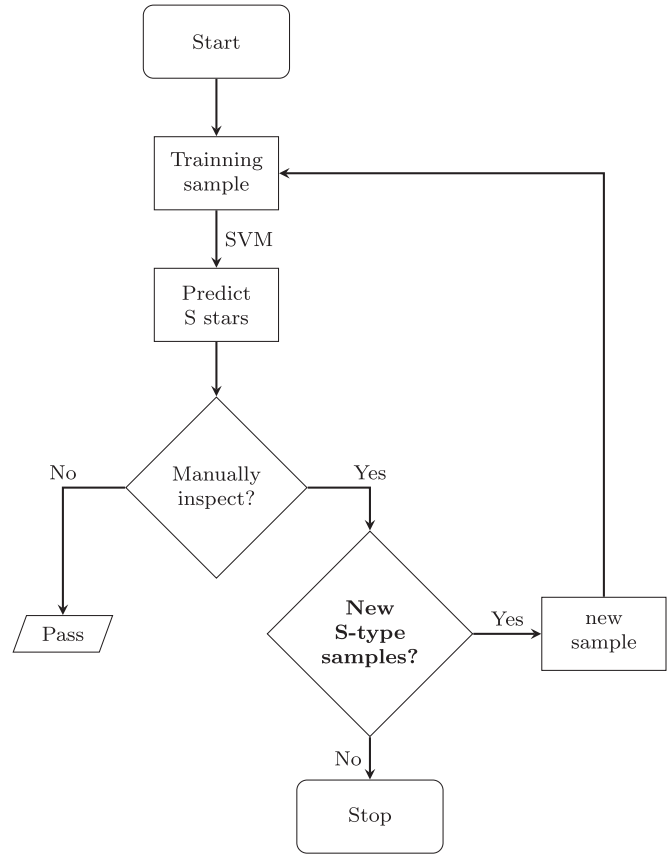

Figure 4. The process of iterative SVM for selecting S-type stars.

samples of the second round. In each subsequent round, we all checked whether there were new S-type stars and put them into the training sample. This cycle did not finish until there were only a few new S-type stars to be found, and 613 S-type stars were finally selected from LAMOST DR9 MRS after five cycles. The specific flowchart of iterative SVM is shown in Figure 4.

3. Further Investigation

3.1. Studying the Evolutionary Stage Using M_{bol}

From the evolutionary point of view, luminous red stars can be divided into two distinct groups: red supergiants (RSG) and AGB stars. The supergiants are burning helium (or carbon) in nondegenerate cores, and they are defined as stars with $M \gtrsim 9M_{\odot}$. The AGB stars have completed core burning and are evolving up the giant branch for the second time, burning hydrogen and helium in shells around an electron-degenerate carbon/oxygen core.

It is difficult to distinguish between AGBs and RSGs because they are both red and luminous. Wood et al. (1983) suggested a criterion to distinguish them: $M_{\rm bol} = -7.1$, which was applied to the 613 S-type stars in this work. We estimated the absolute bolometric magnitude via

$$M_{\rm bol} = M_G + {\rm BC}_G(T_{\rm eff}), \quad (5)$$

where M_G is the absolute magnitude of the G band, and ${\rm BC}_G(T_{\rm eff})$ is the bolometric correction dependent only on temperature. Gaia has defined a function of $BC_G(T_{\rm eff})$ in two

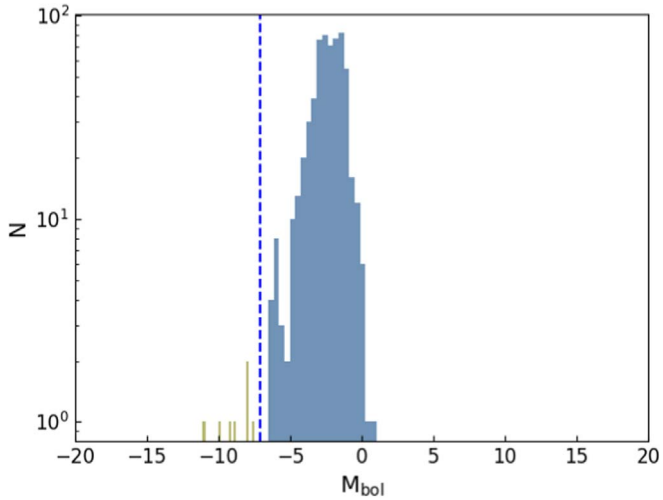

Figure 5. The distribution of the absolute bolometric magnitude for 613 S-type stars. $M_{bol} = -7.1$ is denoted by the dashed blue line.

temperature regions of 2500–4000 K and 4000–8000 K as follows, with different polynomial coefficients, respectively:

$$BC_G(T_{eff}) = \sum_{i=0}^{4} a_i (T_{eff} - T_{eff,\odot}), \quad (6)$$

where a_i is the fitting coefficient, T_{eff} is the temperature of the stars coming from Gaia DR2, and $T_{eff,\odot}$ is the solar temperature, which is set to 5772 K (Prša et al. 2016). Because the temperature of S-type stars is low, we used the coefficients of 2500–4000 K to calculate the bolometric correction.

Figure 5 shows the distribution of the absolute bolometric magnitude for 613 S-type stars, and the dashed line represents $M_{bol} = -7.1$. On the left of the dashed line is the AGB area, on the right is the RSG area, and approximately 99.2% of the 613 S-type stars are in the AGB area. There are seven sources with $M_{bol} < -7.1$; we crossed them with SIMBAD at 3″, and the specific information is shown in Table 4. Although there are two S-type stars in this table, in order to ensure the reliability of the sample, we still removed the seven stars from 613 S-type stars, and the remaining 606 S-type stars were the final sample.

3.2. Studying the Evolutionary Stage Using the CMD

Yang & Jiang (2011) verified 189 RSGs using several CMDs in the near- and mid-infrared bands. Yang et al. (2019) distinguished AGBs and RSGs in the Small Magellanic Cloud with five optical and infrared CMDs, and we studied the evolutionary stage of 613 S-type stars with an infrared CMD to check whether they are in the AGB stage as theoretically predicted.

Aside from the 606 S-type stars, known S-type stars, red giant branch (RGB), RSG, red clump (RC), O-rich AGB (OAGB), C-rich AGB (CAGB), and A, F, G, K, and M stars were selected as background stars in the CMD of this work. The known S-type stars were from the catalog of Chen et al. (2019), which contains 151 extrinsic and 190 intrinsic S-type stars, and the RGBs were collected from Wu et al. (2018), which has 3726 stars with small age and mass uncertainties. OAGB and CAGB stars were from Table 9 and Table 10 of Suh (2021). An RC sample of 92,249 stars was available from Ting et al. (2018), which has only 3% contamination, and 3325 RSGs of Boyer et al. (2011) were collected here. In addition, we also used the A, F, G, and K stars from the "LAMOST LRS Stellar Parameter Catalog of A, F, G, and K Stars"; the sample of M giants and M dwarfs is obtained from S. Li et al. (2022, in preparation). The 613 S-type stars and all background samples were cross-matched with 2MASS and Gaia DR2 to obtain J and K magnitudes and parallax, respectively. Table 5 lists the reference and the numbers before and after the cross-matching.

The left panel of Figure 6 shows the CMD of multiple types of stars, the right panel is an enlargement of the AGB region in the left panel, and we can see that AGB stars can be well distinguished from RGBs and RSGs. The CAGB stars (purple area) are obviously redder than the S-type stars (red area), the OAGB stars are distributed in a relatively large region, and there is no obvious feature on the CMD. The distribution of the 606 predicted S-type stars is consistent with that of known S-type stars. In addition, the red "×" denotes seven stars with $M_{bol} < -7.1$, and we can see that they deviate significantly from most of the S-type stars.

Table 4
Basic Information for the Seven Stars with $M_{bol} < -7.1$

LAMOST Designation	R.A.	Decl.	Main_type[a]	M_{bol} [b]
J024933.43+500850.0	42.389319	50.147238	…	−7.51
J051206.90+454642.7	78.028752	45.778555	Mira	−9.13
J062406.62+172350.7	96.0276	17.397435	…	−7.98
J071157.54+072958.8	107.98979	7.4996732	S*	−8.93
J081035.88+145159.9	122.64954	14.866662	…	−7.87
J204924.70+362039.8	312.35293	36.344402	V*	−9.87
J234430.41+560658.7	356.12675	56.11632	S*	−11.09

Notes.
[a] The main type from SIMBAD.
[b] The absolution bolometric magnitude.

Table 5
Samples of Color–Magnitude Diagram

Class	Reference	Number[a]	Selected Number[b]
Predicted S-type stars	This work	606	606
Known S-type stars	Chen et al. (2019)	341	285
Red Giant Branch	Wu et al. (2018)	3,726	3,726
Red Clump	Ting et al. (2018)	92,249	50,860
Red Supergiant	Boyer et al. (2011)	3,325	3,296
O-rich AGB	Suh (2021)	5,908	3,329
C-rich AGB	Suh (2021)	3,596	2,747
LAMOST AFGK	http://dr7.lamost.org/v2.0/catalog	6,179,327	50,000
M giant and M dwarf	S. Li (2022, in preparation)	77,028	68,514

Notes.
[a] The number of each sample in the reference.
[b] The number after cross-matching with 2MASS and Gaia DR2.

3.3. Identification of S-type Stars with C/O

Due to the limitation of the wavelength range of LAMOST MRS, it is difficult to measure the abundance of C and O. In this work, we used two methods to estimate C/O, one using the

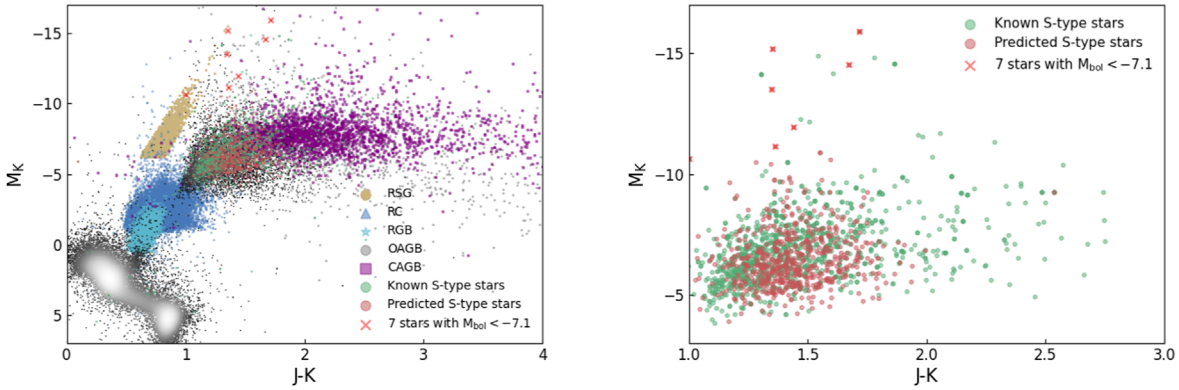

Figure 6. M_K vs. $J-K$ color–magnitude diagram for the samples in Table 5. The yellow dots, blue triangles, blue stars, gray dots, purple squares, green dots, red dots, and red crosses are red supergiants, red clumps, red giant branch stars, O-rich asymptotic giant branch stars, C-rich asymptotic giant branch stars, predicted and known S-type stars, and the seven stars with $M_{bol} < -7.1$, respectively. The color-coded density distribution denotes the LAMOST A, F, G, K, and M stars. The right panel is an enlargement of the known and predicted S-type star region in the left panel.

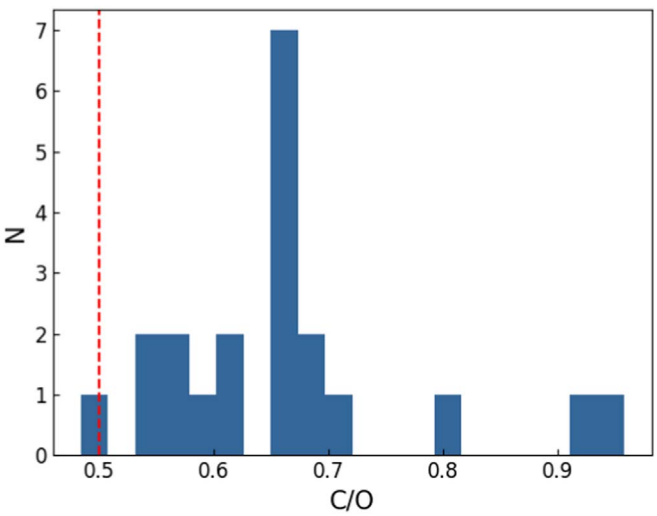

Figure 7. The C/O distribution of 21 S-type stars estimated by the [C/Fe] and [O/Fe] of APOGEE DR16, and the C/O = 0.5 is denoted by the red dashed line.

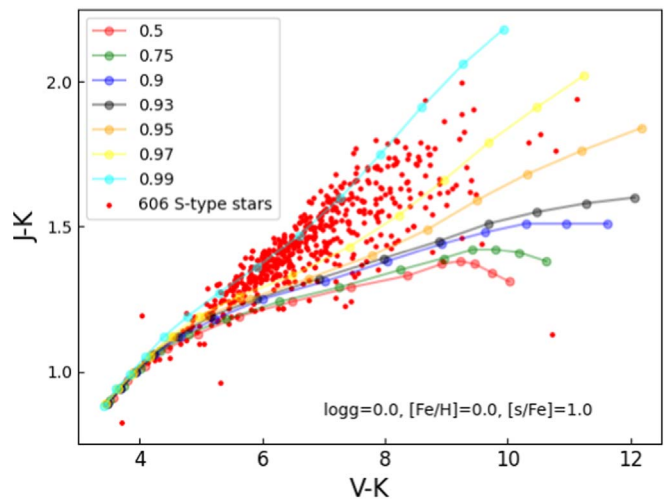

Figure 8. Dereddened $V-K$ and $J-K$ diagram for the 606 S-type stars, as compared to the model colors of different C/O (Van Eck et al. 2017).

C and O abundance from APOGEE, and the other using ($V-K$, $J-K$) photometric indices matching.

APOGEE (Holtzman et al. 2015; Majewski et al. 2017) is a medium-high-resolution ($R \sim 22{,}500$) spectroscopic survey in three near-infrared spectral ranges (1.51–1.70 μm), allowing us to determine the precise atmospheric parameters and chemical abundances even in highly extinct regions. We cross-matched the 606 S-type stars with APOGEE DR16, got the [C/Fe] and [O/Fe] of 21 common stars, and calculated their C/O following the method in Brewer & Fischer (2016). The C/O distribution of the 21 common stars is shown in Figure 7; there is only one star with $C/O < 0.5$, and its C/O is 0.48.

Van Eck et al. (2017) provided a MARCS S-type star model, which constructed a relationship between $V-K$ and $J-K$ for synthetic spectra with C/O = 0.5, 0.75, 0.90, 0.92, 0.95, 0.97, and 0.99, and we used $V-K$ and $J-K$ to estimate the C/Os for the 606 S-type stars. The J and K magnitudes can be obtained through the Point Source Catalog of 2MASS, which contains 470,992,970 sources, and the V magnitude was transformed from magnitudes in the g and r bands using the method from Zhao & Newberg (2006). The g and r magnitudes can come from Panoramic Survey Telescope and Rapid Response System 1 (Pan-STARRS 1; Chambers et al. 2019), which observes the entire sky north of Decl. $= -30°$ (the 3π survey) in *grizy*. We cross-matched the 606 S-type stars with 2MASS and Pan-STARRS using a radius of 3″ and get their J, K, g, and r magnitudes.

The extinction of J, K, g, and r magnitudes was estimated by the Python package dustmaps,[5] which needs the heliocentric distances, R.A., and decl. as inputs (Green et al. 2019). The dereddened $J-K$ and $V-K$ for 606 S-type stars are shown in Figure 8, and the colors of the MARCS S-type star models with different C/Os are also shown in Figure 8. Then, the distances between the dereddened colors ($J-K$ and $V-K$) of the 606 S-type stars and the MARCS models with different C/Os were calculated, and the C/O of the model with the shortest distance was regarded as the C/O of each S-type star. The distribution of the C/O of the 606 S-type stars is shown in Figure 9, and we can see that most of the C/O values are larger than 0.9 as expected, which confirms the reliability of the 606 S-type stars to some extent.

[5] https://pypi.org/project/dustmaps

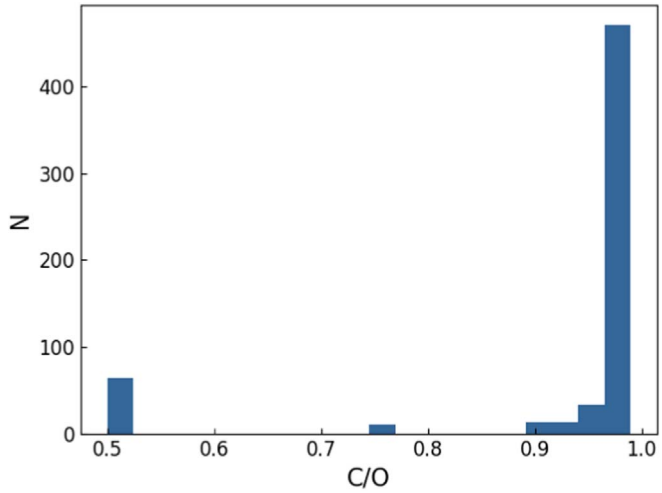

Figure 9. The C/O distribution of 606 S-type stars estimated by the MARCS S-type star model (Van Eck et al. 2017), which constructed a relationship between $V - K$ and $J - K$ for synthetic spectra with C/O = 0.5, 0.75, 0.90, 0.92, 0.95, 0.97, and 0.99.

3.4. Cross-match with the SIMBAD

SIMBAD is the acronym for Set of Identifications, Measurements and Bibliography for Astronomical Data, which is a dynamic database and update every working day. The purpose of Simbad is to provide information on astronomical objects of interest that have been studied in the literature.

TOPCAT was used to cross-match 606 S-type stars with SIMBAD using a radius of 3″; 380 stars had already been reported in the literature, and their detailed information is shown in Table 6. The first and second columns of this table list the main type and other types of the 380 stars, and we can see that they were divided into 12 main types. The third column represents the number of each main type, and the extended explanations of each main type are shown in the notes. From the main type column, a fraction of the 380 stars are indeed variables as expected.

In Table 6, there are 64 S-type stars identified in the literature and 3 S-type candidates. After a further check, 63 of the 64 stars were included in the eight S-type star catalogs of Section 2.2, the remaining 1 was classified as an S-type star by Wright et al. (2009) based on near-IR spectra, and 3 S candidates were reported in Dolidze (1975). Thus, except for the above 67 S-type stars/candidates, the other 539 were first reported as S-type stars in this work.

3.5. The Catalog of S-type Stars

After the above further identifications, we constructed a catalog of 24 columns to list parameters for the 606 S-type stars in Table 7. In this table, only 21 rows of the catalog are shown, which are sorted according to the C/O measured by APOGEE. The full catalog is available from the link:10.12149/101097 or in machine-readable format in Table 8. For convenience, we have divided this table into two parts in the paper. The upper part of the table mainly includes the information we calculated, and the bottom part shows the result after cross-matching with Gaia DR2 and 2MASS. The three columns "TiO", "ZrO," and "class" in the table will be discussed in Section 4. The "–" indicates no measurement.

Table 6
The Information from SIMBAD for the 380 Stars

main_type	Other_types	Number
Star[a]	* | IR	126
V*[b]	* | IR*	71
S*[c]	LP* | V* | IR | *	64
LPV*[d]	* | LP* | V* | IR	59
Candidate.LP*[e]	* | IR | V*	41
Mira[f]	LP* | V* | IR | *	10
Candidate.S*[g]	S*? | IR | * | S*	3
AGB*[h]	LP* | V* | IR | *	1
NIR[i]	* | IR	2
Candidate.C*[j]	C*? | IR | *	1
Candidate.EB*[k]	* | IR*	1
Orion.V* [l]	Or* | V* | IR	1

Notes.
[a] Star.
[b] Variable star.
[c] S-type star.
[d] Long-period variable star.
[e] Long-period variable candidate.
[f] Variable star of Mira Cet type.
[g] Possible S-type star.
[h] Asymptotic giant branch star.
[i] Near-infrared source.
[j] Possible carbon star.
[k] Eclipsing binary candidate.
[l] Variable star of Orion type.

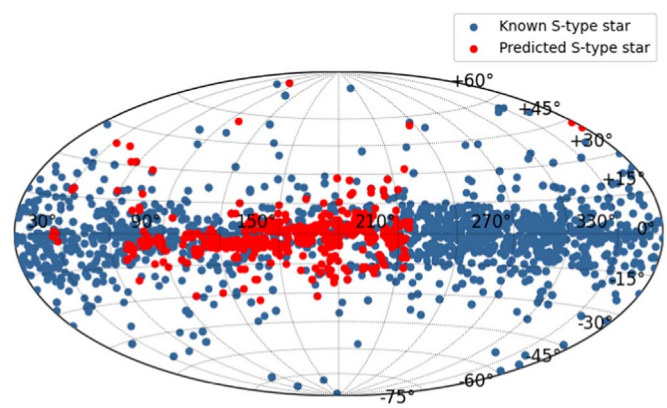

Figure 10. The spatial distribution of the 606 S-type stars in the Galactic coordinates.

The spatial distribution of the 606 S-type stars in Galactic coordinates is plotted in Figure 10, and the red and blue dots represent the predicted and known S-type stars, respectively. In the direction of galactic latitude, the distribution of the two samples of stars is relatively consistent, and they are both within $-15° < b < +15°$. In the galactic longitude direction, the known S-type stars are distributed from 0° to 360°, and the S-type stars in this work are mainly focused on the range of $60° < l < 210°$.

4. Discussion

4.1. Analyzing the Effect of TiO and Atmospheric Parameters on ZrO

Figure 11 shows the example spectra of an M-type, an S-type, and a carbon star from top to bottom, and the left and

Table 7
The S-type Star Catalog Constructed in This Work

LAMOST Designation[a] (1)	R.A. (2)	Decl. (3)	Median S/N (4)	TiO (5)	ZrO (6)	Class (7)	$C/O_{(A)}$ (8)	$C/O_{(M)}$ (9)	M_{bol} (10)	main_type (11)	Sptype (12)	Parallax (13)	e_parallax (14)	G (15)	G_{BP} (16)	G_{RP} (17)	BP – RP (18)	Jmag (19)	e_Jmag (20)	Hmag (21)	e_Hmag (22)	Kmag (23)	e_Kmag (24)
J041801.06+603312.0	64.5044480	60.55333400	34	0.06	0.33	…	0.48	0.99	−1.18	Star		0.184	0.067	13.50	15.71	12.14	3.56	9.62	0.02	8.43	0.02	8.04	0.02
J060547.07+243455.7	91.4461640	24.58215800	143	0.13	0.27	E	0.53	0.99	−2.21	Star		0.278	0.080	11.51	13.36	10.23	3.13	8.04	0.02	7.02	0.02	6.64	0.02
J025505.05+532412.2	43.7710510	53.40341600	23	0.21	0.26	E	0.55	0.99	−2.15	V*		0.235	0.070	12.04	14.01	10.73	3.29	8.50	0.03	7.43	0.02	7.07	0.03
J065944.76+041148.4	104.9365400	4.19678180	59	0.20	0.26	…	0.57	0.97	−1.99	Star		0.328	0.080	11.43	13.24	10.16	3.08	8.09	0.03	7.19	0.04	6.78	0.02
J062437.77+221951.7	96.1573890	22.33104800	32	0.21	0.28	…	0.58	0.97	−1.67	V*		0.190	0.175	13.01	15.64	11.57	4.07	8.85	0.03	7.62	0.05	7.22	0.02
J004700.39+583122.1	11.7516590	58.52283000	34	0.15	0.26	E	0.59	0.99	−1.47	Star	M3	0.377	0.076	11.58	13.33	10.34	2.99	8.27	0.03	7.37	0.06	6.99	0.02
J064024.65+234358.4	100.1027400	23.73289400	208	0.04	0.40	E	0.60	0.97	−2.88	S*	S	0.234	0.072	10.98	12.45	9.85	2.60	8.08	0.02	7.24	0.10	6.85	0.02
J074420.24+163110.6	116.0843400	16.51962400	94	0.12	0.30	E_L	0.62	0.93	−4.26	V*		0.058	0.051	12.63	13.93	11.54	2.39	9.92	0.02	9.07	0.02	8.77	0.02
J045324.01+490003.5	73.3500680	49.00097300	95	0.03	0.49	E	0.66	0.99	−1.34	V*		0.294	0.080	12.38	14.66	11.05	3.61	8.73	0.03	7.61	0.03	7.18	0.03
J052710.36+262539.0	81.7931860	26.42752000	32	0.03	0.35	…	0.66	0.99	−3.23	V*		0.078	0.080	13.35	15.24	12.06	3.17	9.80	0.02	8.65	0.03	8.28	0.03
J061403.24–054335.7	93.5135200	−5.72658700	50	0.20	0.34	…	0.66	0.99	−5.87	…	…	0.033	0.084	12.58	14.61	11.29	3.32	9.18	0.03	8.14	0.02	7.75	0.03
J053357.01+320446.3	83.4875780	32.07953600	26	0.04	0.34	…	0.66	0.99	−3.82	…	…	0.040	0.087	14.23	16.81	12.79	4.02	10.02	0.02	8.80	0.02	8.30	0.02
J042645.72+495356.6	66.6905140	49.89907400	72	−0.03	0.35	…	0.66	0.99	−1.12	Star	.	0.212	0.106	13.14	15.31	11.79	3.52	9.18	0.03	7.96	0.05	7.52	0.03
J192453.00+382740.2	291.2208500	38.46118500	52	0.21	0.25	…	0.66	0.75	−2.24	LPV*		0.311	0.058	11.34	13.11	10.08	3.04	8.07	0.02	7.18	0.02	6.88	0.02
J041027.17+275343.8	62.6132300	27.89551000	250	0.08	0.33	E_L	0.67	0.97	−2.99	V*		0.159	0.047	11.95	13.48	10.77	2.71	8.98	0.02	8.09	0.06	7.75	0.03
J024840.34+522851.1	42.1681200	52.48087700	80	−0.02	0.40	…	0.68	0.97	−1.42	Star	.	0.222	0.042	12.55	14.00	11.41	2.58	9.61	0.02	8.69	0.03	8.39	0.02
J063403.50+230152.3	98.5145980	23.03119700	164	0.10	0.34	…	0.68	0.9	−2.21	Star		0.338	0.088	10.98	12.49	9.83	2.67	8.00	0.03	7.09	0.02	6.80	0.02
J044915.36+444614.8	72.3140290	44.77078600	141	−0.02	0.32	E	0.70	0.99	−1.07	Star		0.342	0.059	12.06	13.71	10.85	2.87	8.74	0.03	7.69	0.03	7.33	0.02
J042243.70+172919.7	65.6821190	17.48880900	95	0.11	0.38	E	0.81	0.97	−2.12	Candidate_LP*		0.204	0.100	12.38	14.44	11.08	3.36	8.89	0.02	7.96	0.02	7.55	0.02
J054344.26+143843.3	85.9344190	14.64536600	49	−0.02	0.44	…	0.92	0.99	−2.36	Star		0.213	0.060	11.95	13.68	10.74	2.94	8.74	0.02	7.74	0.02	7.38	0.02
J061207.47–063700.2	93.0311400	−6.61672300	80	0.18	0.32	E_L	0.96	0.99	−3.66	V*		0.117	0.076	12.04	14.14	10.72	3.42	8.50	0.02	7.43	0.03	7.07	0.02

Notes.
Column (1): The designation from LAMOST DR9.
Column (4): The median value of all pixel S/Ns in the single-exposure red-band spectrum, which is the highest S/N in multiple epochs for one star.
Columns (5) and (6): The band indices of TiO and ZrO obtained from the red-band spectrum with the highest S/N, discussed in Section 4.
Column (7): The class of binary candidates, discussed in Section 4.
Column (8): The C/O estimated by the [C/Fe] and [O/Fe] from APOGEE.
Column (9): The C/O estimated by the MARCS S-type star model.
Column (10): The absolute bolometric magnitude.
Columns (11) and (12): The main type and spectral type from SIMBAD.
Columns (13)–(18): The parallax and uncertainty, the three broadband magnitudes, and the BP – RP color from Gaia DR2.
Columns (19)–(24): The *J*, *H*, and *K* magnitudes and their uncertainties from 2MASS.

(This table is available in its entirety in machine-readable form.)

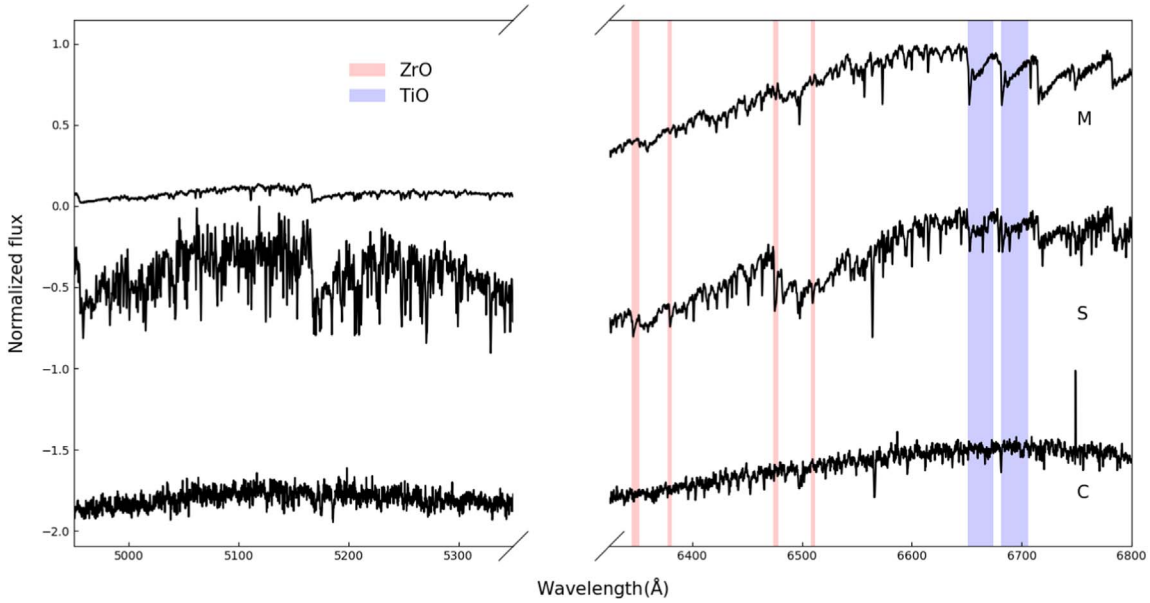

Figure 11. From top to bottom, the spectra of the M-S-C evolution sequence are represented. The M-type stars have strong TiO bands, the S-type stars have strong ZrO and relatively weak TiO, and both ZrO and TiO bands are disappeared in the carbon star. The red and blue areas are ZrO and TiO bands, respectively.

Table 8
Boundaries of the Continuum and Band Windows of TiO Used in the Computation of the Band Indices

Band	$\lambda_{B,i}$	$\lambda_{B,f}$	$\lambda_{C,i}$	$\lambda_{C,f}$
TiO_1	6651.0	6674.0	6646.0	6650.0
TiO_2	6681.0	6706.0	6646.0	6650.0

right parts are their blue- and red-band spectra, respectively. It can be seen from the figure that there are no obvious spectral features at the blue-band spectra, both ZrO (red area) and TiO (purple area) are obvious in the red-band spectra, and the ZrOs of S-type stars are much stronger.

The TiO-band indices of the 606 S-type stars were calculated in the same way as those of ZrO, which are also included in our S-type star catalog in Table 7, and the band and continuum windows are listed in Table 8. For comparison, the TiO- and ZrO-band indices of 1000 M giants from S. Li et al. (2022, in preparation) were also estimated, and the two indices of the 606 S-type stars and 1000 M giants are displayed in Figure 12. It should be noted that the TiO- and ZrO-band indices of each S-type star and M giant were calculated by the red-band spectrum with the highest S/N. From this figure, the TiO indices of S-type stars and M giants are overlapped in the range of [−0.4, 0.4], and the ZrOs of S-type stars are obviously stronger than those of M-giant stars. The TiO- and ZrO-band indices of M giants are mainly distributed in the range of [0.0, 0.25] and [0.1, 0.3], respectively, and there is an obviously positive correlation between ZrO and TiO for M giants. The two band indices for S-type stars mainly focus on the range of [0.0, 0.3] and [0.25, 0.5]; there are still a few S-type stars located near TiO = −0.2 and ZrO = 0.6, and there may be a negative correlation between ZrO and TiO for S-type stars, which needs more S-type star samples to verify.

The "LAMOST DR9 Parameter Catalog" provides the atmospheric parameters of $T_{\rm eff}$, log g, and [Fe/H] for a fraction of the LAMOST MRS spectra. The 606 S-type stars were cross-matched with the catalog, and the $T_{\rm eff}$, log g, and [Fe/H] of 288 stars were obtained. The effect of $T_{\rm eff}$, log g, and [Fe/H] on the ZrO of the 288 S-type stars were analyzed, and we found that log g seems to have the greatest effect on ZrO. The $T_{\rm eff}$ of the 288 S-type stars were divided into two bins of [3200 K, 3500 K] and [3500 K, 4100 K], their [Fe/H] were divided into two ranges of >-0.1 and <0.1, and the 288 stars were clustered into four groups according to different $T_{\rm eff}$ and [Fe/H] ranges. The log g and ZrO indices for stars of each group were fitted with the first-order polynomials, which are shown by different color lines in Figure 13, and the four fitting functions are displayed in the legend. As can be seen from this figure, log g has a negative correlation with ZrO for the four groups of stars, the slopes of the fitting polynomials are much steeper for the two groups of warmer stars, and $T_{\rm eff}$ and [Fe/H] have little effect on ZrO. In the future, more S-type stars with accurate atmospheric parameters are needed to further investigate the effects of atmospheric parameters on ZrO.

4.2. Binary Candidates

The "LAMOST MRS general catalog" provides the RVs of blue- and red-band spectra, and the RVs were calibrated by the radial velocity standard stars provided in Huang et al. (2018). Chen et al. (2021) compared the RVs of 9110 objects in both LAMOST and SDSS14/APOGEE, and the dispersion is only around 1 km s^{-1}. In addition, Zhang et al. (2021) measured the RVs of 3.8 million single-exposure spectra (about 0.6 million stars) of LAMOST MRS with S/Ns greater than 5 and propose a robust method to determine the RV zero-point, which has an average accuracy of 0.38 km s^{-1}. Because the coadded spectra of LAMOST MRS are the results of manual processing, which may introduce inevitable problems, we only use the RVs of single exposure spectra for analysis. Due to the spectrum characteristics of S-type stars being mainly in the red band, the RVs after zero-point calibrations are all provided in the "LAMOST MRS general catalog" and Zhang et al. (2021), and only the calibrated RVs of the red-band spectra (RV_red_{LAMOST} and RV_red_{Zhang}) were used.

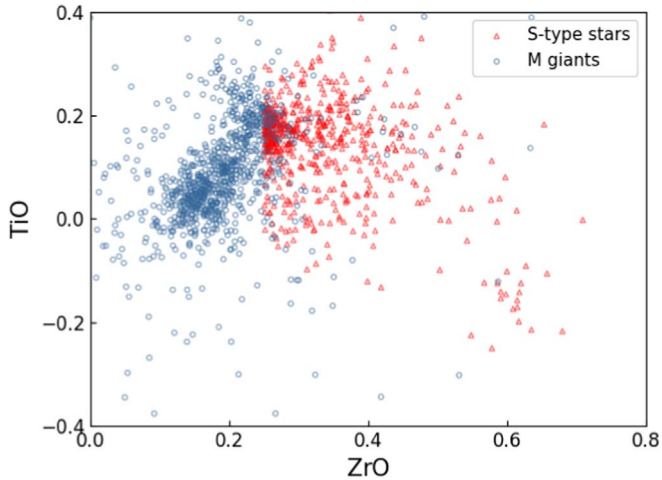

Figure 12. Measured $B_{\rm ZrO}$- and $B_{\rm TiO}$-band indices of the 606 S-type stars (red) and 1000 M giants (blue), respectively.

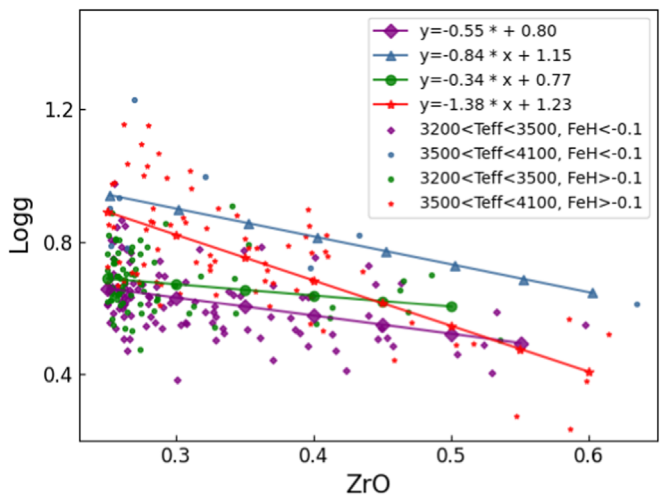

Figure 13. The surface gravity vs. ZrO for the 288 S-type stars with atmospheric parameters given by LAMOST. The points and lines with different colors represent four groups of S-type stars and their fitting results with the first-order polynomials, respectively.

We cross-matched the 606 S-type stars with the "LAMOST MRS general catalog" and the catalog of Zhang et al. (2021), obtained the RV_red$_{\rm LAMOST}$ and RV_red$_{\rm Zhang}$ of 8728 single-exposure spectra of 506 stars, and spectra with RV $= -9999$ km s^{-1} were excluded. The comparison of RV_red$_{\rm LAMOST}$ and RV_red$_{\rm Zhang}$ for 506 stars is shown in the top panel of Figure 14, and they are relatively consistent. The bottom panel shows the difference distribution of RV_red$_{\rm LAMOST}$ and RV_red$_{\rm Zhang}$, and the offset and dispersion of the difference are -0.8 km s^{-1} and 3.3 km s^{-1}, respectively, when $|{\rm RV\_red_{LAMOST}} - RV\_{\rm red_{Zhang}}| < 40$ km s^{-1}.

Tian et al. (2020) used $\Delta{\rm RV_{max}} > 3.0\ \sigma_{\rm RV}$ to identify binary stars, where ΔRV is the RV difference between any two epochs for an object, $\Delta{\rm RV_{max}}$ is the maximum of ΔRV, and $\sigma_{\rm RV}$ is the standard deviation of multiple epochs. We used RV_red$_{\rm LAMOST}$ and RV_red$_{\rm Zhang}$ to calculate the ΔRV and $\Delta{\rm RV_{max}}/\sigma_{\rm RV}$ for 506 S-type stars, which are shown in Figure 15. According to the criterion of $\Delta{\rm RV_{max}} > 3.0\ \sigma_{\rm RV}$, there are a total of 238 binary candidates found by RV_red$_{\rm LAMOST}$ and RV_red$_{\rm Zhang}$, and they are marked in the "class" column of Table 7 using "E", "E$_{\rm L}$," and "E$_{\rm Z}$", which

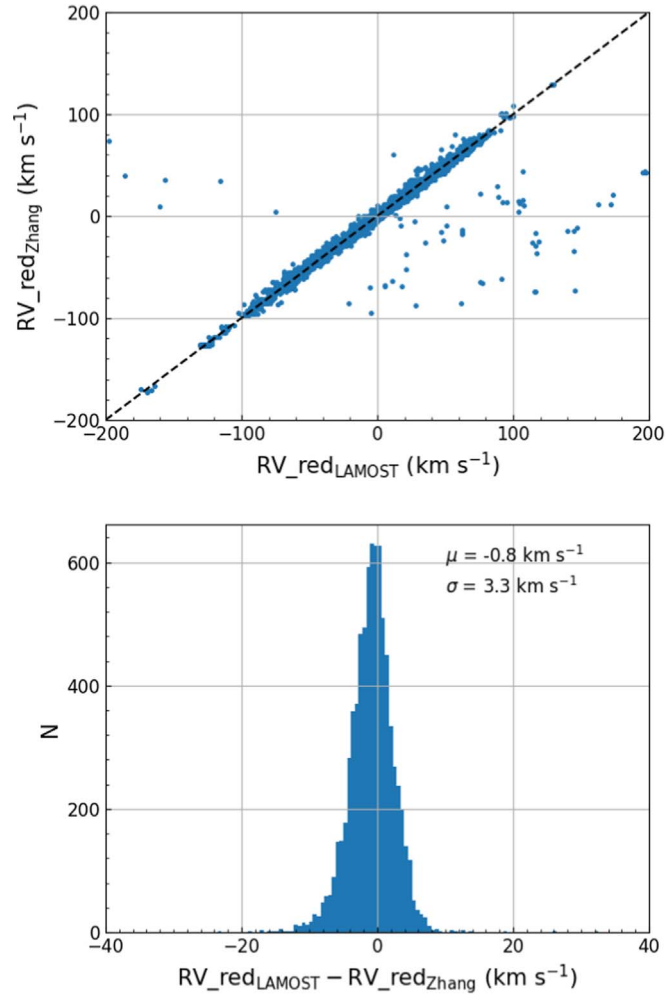

Figure 14. The RV comparison of red-band spectra from the "LAMOST MRS general catalog" and the catalog in Zhang et al. (2021) (RV_red$_{\rm LAMOST}$ and RV_red$_{\rm Zhang}$). The top panel shows the point-to-point comparisons of RV_red$_{\rm LAMOST}$ and RV_red$_{\rm Zhang}$, and the distribution of their difference is shown in the bottom panel.

denote that they were classified as extrinsic S-type (binary) candidates using both RV_red$_{\rm LAMOST}$ and RV_red$_{\rm Zhang}$, only RV_red$_{\rm LAMOST}$, or only RV_red$_{\rm Zhang}$, respectively. Among the 238 binary candidates, there are 127, 73, and 38 stars classified as "E", "E$_{\rm L}$," and "E$_{\rm Z}$", respectively, and the 127 stars with class "E" are more likely to be binary candidates because they satisfy the criterion of Tian et al. (2020) no matter RV_red$_{\rm LAMOST}$ or RV_red$_{\rm Zhang}$ used. "–" in the "class" column represents the other stars that were not considered binary candidates in this work, due to the relatively few observations or the relatively low accuracies of the RV measurements.

5. Summary

In this paper, we preliminarily selected S-type star candidates from the low-temperature-giant sample of LAMOST DR9 using the criterion of ZrO-band indices and further used the iterative SVM algorithm to select S-type stars from the candidates, and 613 S-type stars were finally selected after the iterative SVM. We investigate these stars, and the main conclusions are:

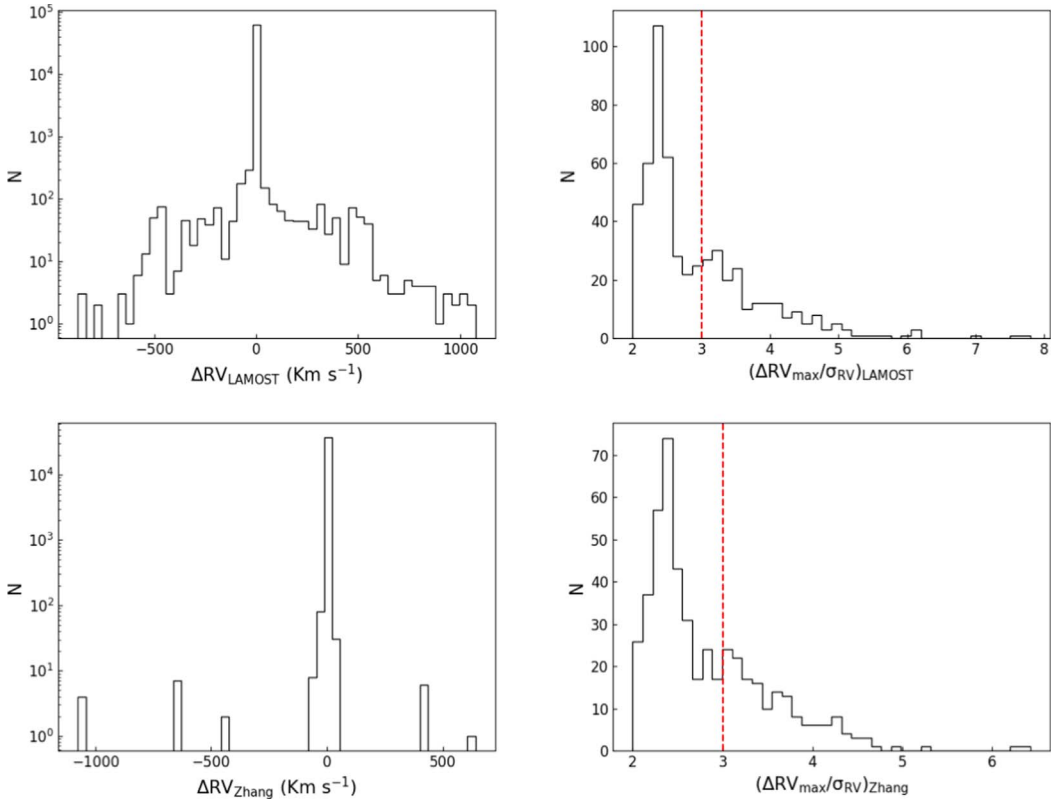

Figure 15. The top and bottom panels give the distributions of ΔRV and $\Delta RV_{max}/\sigma_{RV}$ estimated by RV_red$_{LAMOST}$ and RV_red$_{Zhang}$ (introduced in Figure 14), respectively, where ΔRV is the RV difference between any two epochs for an object, ΔRV_{max} is the maximum of ΔRV, and σ_{RV} is the standard deviation of multiple epochs. The red dashed line denotes the criterion of $\Delta RV_{max} = 3.0\,\sigma_{RV}$ for selecting binary candidates.

1. In general, the absolute bolometric magnitude of S-type stars is larger than -7.1 (Wood et al. 1983). We calculated the M_{bol} for 613 S-type stars and found there were 7 stars with $M_{bol} < -7.1$. The remaining 606 stars were our final S-type samples, 67 S-type stars/candidates among them were already identified in the literature through cross-matching with SIMBAD, and the other 539 stars are first reported in this paper. In the CMD of ($J-K$) and M_K, the 606 S-type stars are distributed in the AGB stage and are also consistent with the distribution of known S-type stars.
2. We used two methods to evaluate the C/O of 606 S-type stars. First, the C/Os of 21 S-type stars were obtained by the C and O abundances from APOGEE DR16 and 20 of them have C/O > 0.5. Second, an MARCS model of S-type stars is provided by Van Eck et al. (2017), which can be used to estimate C/O (from 0.5 to 0.99) with $V-K$ and $J-K$, the C/Os of 606 S-type stars were estimated with this model, and most of the C/O values are larger than 0.9.
3. The band indices of TiO and ZrO for 606 S-type stars and 1000 M giants were calculated. There may be a negative correlation between ZrO and TiO for S-type stars, which is different from the obvious positive correlation of the two bands for M giants. In addition, the effects of atmospheric parameters on ZrO were analyzed, log g has a negative correlation with ZrO, which has the greatest effect on ZrO compared with T_{eff} and [Fe/H], and the slopes of the negative correlation are much steeper for warmer stars. More S-type stars are needed in the future to verify the relationship of TiO versus ZrO, and log g versus ZrO.
4. We cross-matched 606 S-type stars with "the LAMOST MRS general catalog" and the catalog of Zhang et al. (2021) and got 506 common stars with the zero-point-calibrated RVs of the red-band spectra (RV_red$_{LAMOST}$ and RV_red$_{Zhang}$). According to the criterion of Tian et al. (2020), there are a total of 238 binary candidates found by RV_red$_{LAMOST}$ and RV_red$_{Zhang}$.

We constructed a catalog for 606 S-type stars, which includes 24 columns such as the band indices of TiO and ZrO, the C/Os obtained by two methods, and the cross-matched results with SIMBAD, Gaia, and 2MASS, and it is available from 10.12149/101097 and Table 8.

We thank the anonymous referee for valuable comments and suggestions. We also thank Guo Yan-Xin and Kong Xiao for helpful discussions. This work is supported by the National Science Foundation of China (Nos. U 1931209, 12003050) and the National Key R&D Program of China (No. 2019YFA 0405502), China Manned Space Project (Nos. CMS-CSST-2021-A10, CMS-CSST-2021-B05). Guoshoujing Telescope (the Large Sky Area Multi-Object Fiber Spectroscopic Telescope, LAMOST) is a National Major Scientific Project built by the Chinese Academy of Sciences. Funding for the project has been provided by the National Development and Reform Commission. LAMOST is operated and managed by the National Astronomical Observatories, the Chinese Academy of Sciences. This research makes use of data from the European Space Agency (ESA) mission Gaia, processed by the

Gaia Data Processing and Analysis Consortium. This research also makes use of Astropy, a community-developed core Python package for Astronomy (Astropy Collaboration et al. 2013), the TOPCAT tool (Taylor 2005), and the VizieR catalog access tool and the Simbad database, operated at CDS, Strasbourg, France.

ORCID iDs

Jing Chen https://orcid.org/0000-0001-8869-653X
A-Li Luo https://orcid.org/0000-0001-7865-2648
Yin-Bi Li https://orcid.org/0000-0001-7607-2666
Xiang-Lei Chen https://orcid.org/0000-0001-5738-9625
Rui Wang https://orcid.org/0000-0001-6767-2395
Shuo Li https://orcid.org/0000-0002-8913-3605
Bing Du https://orcid.org/0000-0001-6820-6441
Xiao-Xiao Ma https://orcid.org/0000-0002-9279-2783

References

Ake, T. B. 1979, ApJ, 234, 538
Astropy Collaboration, Robitaille, T. P., Tollerud, E. J., et al. 2013, A&A, 558, A33
Blanco, V. M., & Nassau, J. J. 1957, ApJ, 125, 408
Boyer, M. L., Srinivasan, S., van Loon, J. T., et al. 2011, AJ, 142, 103
Brewer, J. M., & Fischer, D. A. 2016, ApJ, 831, 20
Chambers, K. C., Magnier, E. A., Metcalfe, N., et al. 2019, arXiv:1612.05560
Chen, P. S., Liu, J. Y., & Shan, H. G. 2019, AJ, 158, 22
Chen, X.-L., Luo, A. L., Chen, J.-J., et al. 2021, PASP, 133, 044502
Cortes, C., & Vapnik, V. 1995, Mach. Learn., 20, 273
Cui, X.-Q., Zhao, Y.-H., Chu, Y.-Q., et al. 2012, RAA, 12, 1197
Dolidze, M. V. 1975, AbaOB, 47, 3
Gaia Collaboration, Prusti, T., de Bruijne, J. H. J., et al. 2016, A&A, 595, A1
Gaia Collaboration, Brown, A. G. A., Vallenari, A., et al. 2018, A&A, 616, A1
Gałan, C., Mikołajewska, J., Monard, B., et al. 2019, AcA, 69, 25
Green, G. M., Schlafly, E., Zucker, C., Speagle, J. S., & Finkbeiner, D. 2019, ApJ, 887, 93
Gustafsson, B., Edvardsson, B., Eriksson, K., et al. 2008, A&A, 486, 951
Henize, K. G. 1960, AJ, 65, 491
Holtzman, J. A., Shetrone, M., Johnson, J. A., et al. 2015, AJ, 150, 148
Huang, Y., Liu, X. W., Chen, B. Q., et al. 2018, AJ, 156, 90
Iben, I. J, & Renzini, A 1983, ARA&A, 21, 271
Jorissen, A., & Mayor, M. 1988, A&A, 198, 187
Keenan, P. C. 1954, ApJ, 120, 484
Luo, A. L., Zhang, H.-T., Zhao, Y.-H., et al. 2012, RAA, 12, 1243
MacConnell, D. J. 1979, A&AS, 38, 335
Majewski, S. R., Schiavon, R. P., Frinchaboy, P. M., et al. 2017, AJ, 154, 94
Merrill, P. W. 1922, ApJ, 56, 457
Plez, B., van Eck, S., Jorissen, A., et al. 2003, in IAU Symp. 210, Modelling of Stellar Atmospheres, ed. N. Piskunov, W. W. Weiss, & D. F. Gray (Cambridge: Cambridge Univ. Press), A2
Prša, A., Harmanec, P., Torres, G., et al. 2016, AJ, 152, 41
Raskin, G., van Winckel, H., Hensberge, H., et al. 2011, A&A, 526, A69
Shetye, S., Goriely, S., Siess, L., et al. 2019, A&A, 625, L1
Shetye, S., Van Eck, S., Goriely, S., et al. 2020, A&A, 635, L6
Shetye, S., Van Eck, S., Jorissen, A., et al. 2018, A&A, 620, A148
Smith, V. V., & Lambert, D. L. 1990, ApJS, 72, 387
Stephenson, C. B. 1976, PW&SO, 2, 2
Stephenson, C. B. 1984, PW&SO, 3, 1
Stephenson, C. B. 1990, AJ, 100, 569
Su, D.-Q., & Cui, X.-Q. 2004, ChJAA, 4, 1
Suh, K.-W. 2021, ApJS, 256, 43
Taylor, M. B. 2005, in ASP Conf. Ser. 347, Astronomical Data Analysis Software and Systems XIV, ed. P. Shopbell, M. Britton, & R. Ebert (San Francisco, CA: ASP), 29
Tian, Z., Liu, X., Yuan, H., et al. 2020, ApJS, 249, 22
Ting, Y.-S., Hawkins, K., & Rix, H.-W. 2018, ApJL, 858, L7
Van Eck, S., & Jorissen, A. 1999, A&A, 345, 127
Van Eck, S., & Jorissen, A. 2000, A&A, 360, 196
Van Eck, S., Jorissen, A., Udry, S., et al. 2000, A&AS, 145, 51
Van Eck, S., Neyskens, P., Jorissen, A., et al. 2017, A&A, 601, A10
Wang, S.-G., Su, D.-Q., Chu, Y.-Q., Cui, X., & Wang, Y.-N. 1996, ApOpt, 35, 5155
Wood, P. R., Bessell, M. S., & Fox, M. W. 1983, ApJ, 272, 99
Wright, N. J., Barlow, M. J., Greimel, R., et al. 2009, MNRAS, 400, 1413
Wu, Y., Xiang, M., Bi, S., et al. 2018, MNRAS, 475, 3633
Yang, M., & Jiang, B. W. 2011, ApJ, 727, 53
Yang, M., Bonanos, A. Z., Jiang, B.-W., et al. 2019, A&A, 629, A91
Zhang, B., Li, J., Yang, F., et al. 2021, ApJS, 256, 14
Zhao, C., & Newberg, H. J. 2006, arXiv:astro-ph/0612034
Zhao, G., Chen, Y.-Q., Shi, J.-R., et al. 2006, ChJAA, 6, 265
Zhao, G., Zhao, Y.-H., Chu, Y.-Q., Jing, Y.-P., & Deng, L.-C. 2012, RAA, 12, 723
Zinn, J. C., Pinsonneault, M. H., Huber, D., & Stello, D. 2019, ApJ, 878, 136